

HiSST: 4th International Conference on High-Speed Vehicle Science Technology 22 -26 September 2025, Tours, France





Design Study of a 2-dimensional Scramjet Inlet Operating over a Wide Range of Mach Numbers

Masahiro Takahashi¹, Tatsushi Isono², Koichiro Tani³, and Sadatake Tomioka⁴

Abstract

In developing a turbine-based combined cycle engine for a hypersonic cruise transport aircraft, the technical challenge is to extend the operating range of the scramjet engine (SCRJ) to low speeds (expected to be between Mach 3 and 4), enabling switching with the turbo-ramjet engine (TRJ). This study aimed to develop a design method for scramjet inlets that can maintain a suitable flow field for startup conditions down to the low-speed transition point with the TRJ while achieving high inlet performance during high-speed cruising. This involved optimizing the pressure ratio distribution of a two-dimensional, multi-stage ramp mixed-compression inlet, as well as a CFD-based startability evaluation. Optimizing the pressure ratio distribution using the inlet's total pressure recovery (which accounts for viscous losses) as the objective function resulted in a nearly uniform distribution, similar to the inviscid flow case. This occurs because the total pressure loss due to oblique shock waves is dominant while the contribution of viscous losses is small. Next, an inlet designed for an overall pressure ratio of 30 under cruise conditions, assuming a flight Mach number of 6, failed to obtain a start-state flow field under switching conditions from the TRJ, assuming a Mach number of 3.5. Reducing the internal compression ratio while maintaining the same overall pressure ratio allowed the inlet to achieve a start-state flow field. However, reducing the internal compression ratio caused the inlet flow-path to tilt downward, which significantly increased drag, particularly on the outer surface of the cowl.

Keywords: Scramjet inlet, Scramjet engine, Turbine based combined cycle engine, CFD

Nomenclature

Latin

 C_f – Skin friction coefficient

 C_H – Stanton number

H − Entrance height of an inlet

 H_{12} – Shape factor of boundary layer

h – Exit height of an inlet

L – Total length of an inlet

M - Mach number

N – Total number of compression stages

n – index, also exponent of velocity profile

 P_{rat} – Overall pressure ratio of an inlet

 $P_{rat,n}$ – Pressure ratio of n-th compress. stage

 Re_{θ} – Reynolds num. on momentum thickness

s – Coordinate along a wall surface

T – Temperature

u – Velocity

X – Coordinate in axial direction

X – Vector of design variables

 x_n – Exponent when $P_{rat,n}$ to be power of P_{rat}

Y - Coordinate in height direction

y⁺ – Wall coordinate

Greek

 γ – Specific heat ratio (=1.4)

Δs – Shock wave incidence point spacing

 δ – Boundary layer thickness

 δ^* – Displacement thickness of boundary layer

 η_{PT} – Total pressure recovery

 θ – Momentum thickness of boundary layer

 θ_e – Flow angle at an inlet exit (= θ_N)

 ρ – Density

¹ JAXA Kakuda Space Center, Kimigaya, Kakuda, Miyagi 981-1525, Japan, E-mail takahashi.masahiro@jaxa.jp

² JAXA Kakuda Space Center, Kimigaya, Kakuda, Miyagi 981-1525, Japan, E-mail <u>isono.tatsushi@jaxa.jp</u>

³ JAXA Kakuda Space Center, Kimigaya, Kakuda, Miyagi 981-1525, Japan, E-mail <u>tani.koichiro@jaxa.jp</u>

⁴ JAXA Kakuda Space Center, Kimigaya, Kakuda, Miyagi 981-1525, Japan, E-mail <u>tomioka.sadatake@jaxa.jp</u>

Subscripts e – Boundary layer edge

aw - Adiabatic wall

1. Introduction

JAXA proposes air-breathing engines (ABE) each optimized for specific applications. For space transportation, while maintaining a single-stage-to-orbit (SSTO) vehicle as the ultimate common goal, we propose several vehicle and engine configurations tailored to intermediate-stage applications. For example, for winged air-launchers using Two-Stage-To-Orbit (TSTO) vehicles, JAXA proposes a Rocket-Based Combined Cycle (RBCC) engine combining a scramiet engine with a wide operating speed range and a rocket engine [1]. Taking advantage of the potential for smaller vehicle sizes enabled by horizontal takeoff and landing, lift-assisted flight, and the ABE's inherent benefit of reduced onboard oxidizer requirements, the goal is to realize a future space transportation system capable of highly frequent round-trip flights. High-speed point-to-point transportation using this winged vehicle is also attracting attention as a marketable prospect. For one form of this, hypersonic transport aircraft flying at high speeds within the atmosphere, several vehicle concepts incorporating turbo-ramjet engines have been proposed [2, 3]. However, turbo-ramjet engines decelerate the captured supersonic airflow to subsonic speeds within the intake. Consequently, the total pressure loss in the intake increases with higher speeds, limiting practical application to Mach 5. Meanwhile, recent air transport demand studies indicate that travel speeds exceeding Mach 5 could significantly enhance market value [4]. Therefore, JAXA proposes a Turbine-Based Combined Cycle (TBCC) engine for such hypersonic cruise transport aircraft. This engine combines a scramjet (SCRJ) engine, capable of higher-speed flight, with a turboramjet (TRJ) engine to provide thrust from takeoff to the scramjet operating conditions [5].

TRJ engines, which have already been put into practical use up to Mach 3 with engines like the U.S.-developed J58, and SCRJ engines operating in the hypersonic range, whose development for practical application is currently advancing rapidly. To realize a TBCC engine that operates from takeoff to hypersonic speeds by combining these, it is necessary to extend the each engine's operating range in velocity, so that their ranges can overlap and to establish switching technology between them. Therefore, JAXA has initiated a research program in collaboration with several universities to acquire the technologies necessary for realizing the TBCC engine [5]. This research program considers hypersonic cruise transport aircraft as an application for TBCC engines. It is positioned as an extension of current air transport and assumes takeoff and landing from existing airports. Therefore, both the TRJ and SCRJ are designed to operate using jet fuel. The technical challenge for the SCRJ engine in this research program is to extend the operating range of the inlet and combustor down to lower speeds (expected between Mach 3 and 4) to enable switching from the TRJ.

This research aims to develop a design methodology for SCRJ inlets that deliver high performance under cruise conditions while also enabling the capture of airflow required to achieve the sufficient thrust performance during startup at low speeds, along with compression to combustor entrance conditions. Furthermore, the introduction of a variable mechanism is essential to enable switching from the TRJ operation at the low Mach number condition to SCRJ operation across a wide Mach number range. Therefore, considering easier implementation of the variable mechanism, a two-dimensional mixed-compression-type inlet, composed of multiple external and internal compression ramps, was selected as the subject of investigation. In this study, we first determined the pressure ratio distribution for each compression stage configuration to maximize the total pressure recovery, given the overall pressure ratio of the inlet as a design condition for four combinations of external and internal compression ramps. Based on this pressure ratio distribution, we obtained the inlet shape by using oblique shock wave relations and assuming wave-cancellation condition where the incident shock wave does not generate reflected waves. In addition, based on the results, the relationship between the compression stage configuration, pressure ratio distribution, and the performance and shape of the inlet was examined. Note that for inviscid flow, Smart [6] has analytically demonstrated that the pressure ratio distribution maximizing the total pressure recovery for a two-dimensional scramjet inlet results in almost equal pressure ratios for each compression stage of the external compression part and that of the internal compression one. In this study, we estimated wall friction and heat transfer to the wall from inviscid flow conditions calculated using oblique shock wave relations. We then optimized the pressure ratio distribution using a genetic algorithm (GA), with the total pressure recovery accounting for these viscous losses as the objective function, and investigated its impact on the pressure ratio distribution. Next, 2D RANS CFD was applied to the candidate shapes obtained in this manner

after applying correction for boundary layer displacement thickness, and the inlet performance and startability at the design point and off-design points were evaluated.

2. Procedure for design study of scramjet inlet

2.1. Design policy

In recent years, research on highly efficient inlets with 3D flow-path geometries, represented by streamline-tracing inlets, has been active [7, 8]. However, this study focuses on a SCRJ integrated into a TBCC. It assumes that the inlet will also switch via a variable mechanism during the transition from a low-speed TRJ to a high-speed SCRJ, or vice versa. Since variable mechanisms for 3D inlets are too complex, this study selected a 2D multi-stage ramp-compression-type inlet as the subject of investigation. Furthermore, considering the trade-off between achieving high compression ratios and reducing total pressure losses due to shock waves, as well as the startability of the inlet, a mixedcompression-type inlet combining external and internal compression stage was selected.

Next, the design point for the inlet was set for cruise conditions, as it is intended for application to a hypersonic cruise transport aircraft. Here, referencing the aforementioned high-speed transport aircraft demand survey [4], the cruise Mach number was set to 6. The evaluation criteria at non-design points are whether an inlet designed for the highest Mach number within the assumed flight missions possesses a starting solution under low Mach number conditions (non-design points), and whether it can achieve the inlet performance required to meet the thrust level derived from the system studies. Meanwhile, the flight dynamic pressure was set to 50 kPa, a value often assumed in studies of hypersonic air-breathing engines.

Although introducing a variable mechanism is effective for improving inlet performance and expanding the operating range, system feasibility is enhanced by limiting its implementation to the absolute minimum, as it increases system complexity and weight. Therefore, this research first focuses on improving the baseline inlet flow-path geometry without a variable mechanism to maximize air capture efficiency, compression performance, and starting capability. Then, a variable mechanism will be employed to achieve stable starting state preservation and any remaining unmet performance targets. This report discusses the former issue.

2.2. Optimization of pressure ratio distribution to each compression stage using GA and design method for inlet baseline geometries

Fig. 1 shows the schematic of the SCRJ inlet geometry and oblique shock structure evaluated. The inlet geometry was designed as a two-dimensional multi-stage ramp mixed-compression type, consisting of external compression ramps on the upper wall of the inlet flow-path and internal compression ramps on the cowl inner wall. The number of ramps for external compression and that for internal compression, i.e., the number of compression stages, were set to either 2 or 3. Four types of compression stage configurations, as shown in Table 1, were evaluated by combining these two numbers of compression stages. The compression configuration of the inlet shown in Fig. 1 is 2 stages for external compression and 3 stages for internal compression. The inlet total length L is the engine axial distance from the leading edge of the first external compression ramp to the position where the final internal shock wave enters the top wall. The inlet height H is the difference in height between the leading edge of the first external compression ramp and the cowl tip. The exit height h is defined as the flow-path height at the incident point of the final internal shock wave on the top wall.

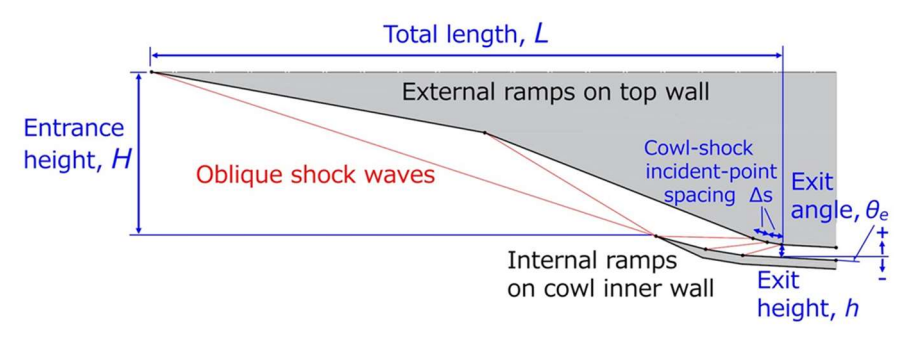


Fig 1. Schematics of a two-dimensional mixed-compression scramjet inlet.

Configuration	133	132	123	122
External compression ramp	3	3	2	2
Internal compression ramp	3	2	3	2

Table 1. Compression stage configuration

In this study, the overall pressure ratio of the inlet, defined by the ratio of static pressure at the inlet exit to that at the inlet entrance, was given as a design condition. Then, the distribution of the pressure ratio to each compression stage was optimized using a genetic algorithm (GA) to determine the inlet flow-path shape. The design variable was defined as the exponent x_n when the pressure ratio of each compression stage $P_{rat,n}$ was expressed as a power of the overall pressure ratio P_{rat} . All values of P_{rat} are positive and less than 1. Furthermore, satisfying the constraint that the sum of P_{rat} equals 1 ensures the overall pressure ratio given as a design condition to be maintained. The objective function was set as the total pressure recovery, calculated from the inlet exit flow conditions, estimated by taking viscous friction loss on the inlet wall and loss due to heat transfer to the wall into account. An optimization problem was formulated to maximize this objective function.

When starting the optimization calculations, results sometimes showed a positive deflection angle for the flow at the inlet exit θ_N , meaning the exit flow was directed upward. Such excessive airflow deflection is undesirable considering the connection to the combustor. Therefore, a penalty function was added to the evaluation function to prevent solutions with a positive exit flow angle θ_N from being selected as the optimal solution.

The optimization problem is formulated as follows. Note that N is the total number of design parameters. In this study, it represents the total number of compression stages, taking integer values from 4 to 6 depending on the compression stage configuration. The population size for each generation was set to either 300 or 500, with 50 generations. The crossover probability was set to 0.7, generating the next generation's individuals through arithmetic crossover from two parents. The mutation rate was set to a slightly higher baseline value of 0.2 to maintain diversity, gradually decreasing over generations. As an elite strategy, the top two individuals from each generation were passed on to the next generation.

• Objective function:
$$f(X) = \eta_{PT} \cdot \exp(-20 \max(0, \theta_N))$$
 (1)

where η_{PT} is the total pressure recovery including viscous loss, and θ_N is the deflection angle of the exit flow.

• Design variables:
$$X = (x_1, x_2, \dots, x_N)$$
 (2)

where overall pressure ratio:
$$P_{rat} = P_{rat,1}P_{rat,2}\cdots P_{rat,N} = P_{rat}^{(x_1+x_1+\cdots+x_N)}$$
 (3)

and pressure ratio of *n*-th stage:
$$P_{rat,n} = P_{rat}^{x_n}$$
, $n = 1, 2, \dots, N$ (4)

• Constraints:
$$x_1 + x_2 + \dots + x_N \equiv 1$$
 (5)

$$x_{min} \le x_n \le x_{max}, \ n = 1, 2, \cdots, N \tag{6}$$

$$\theta_N \le 0 \tag{7}$$

where, for the first ramp of both external and internal compressions, x_{min} was set to 0.02 to maintain the compression stage, and 0 for all others allowing no compression stage. In addition, x_{max} was set to 0.4 for all compression stages. However, in the actual calculation, after setting each design variable individually, the sum of all design variables was divided to satisfy Eq. (5). Therefore, x_{min} and x_{max} represent the constraint values when each design variable is set individually.

Next, we describe the method for determining the inlet flow-path shape for the pressure ratio distribution. In this study, assuming inviscid flow, the shock angle and flow deflection angle were calculated using oblique shock relations for the given pressure ratio of each compression stage. For calculating the coordinate of the definition point for the inlet flow-path shape, the following conditions were applied under the design flow conditions.

1. All external shock waves impinge on the leading edge of the cowl (Shock-on-lip condition).

- 2. To prevent reflection waves from forming when oblique shock waves impinge on the opposite side, the upper wall behind the oblique shock wave and the cowl inner wall shall be parallel to the airflow after the oblique shock wave passes (wave-cancellation condition).
- 3. The incident points of each internal shock wave on the top wall shall be spaced at a specified interval Δs .

Here, point 3 is to prevent the occurrence of a large adverse pressure gradient when each internal shock wave incident on a narrow area of the upper wall, causing boundary layer separation and, in the worst case, a transition to inlet-unstart.

Next, from the inviscid flow-path shape obtained by the above method and the airflow conditions in each region separated by oblique shock waves, the friction drag generated on the upper wall and the cowl inner wall and the heat transfer to the wall surfaces were estimated. These were integrated along each wall surface to determine the total loss of momentum and energy, which were then used to correct the inviscid exit airflow conditions. Then, the total pressure recovery was calculated from these exit flow conditions, which considered the viscous losses, and used for the objective function. The friction coefficient C_f used to estimate the friction drag was calculated using the Van Driest II method [9]. In addition, the Stanton number C_H used to estimate heat transfer was obtained by assuming Reynolds analogy from the friction coefficient C_f . The Reynolds analogy factor $C_H/(C_f/2)$ was assumed to be 1 [10].

GA optimization was applied for each of the four compression forms to find the optimal solution for each.

2.3. Correction for boundary layer displacement thickness

The inlet baseline geometry determined using the method described in Section 2.2 employs the total pressure recovery, which accounts for viscous losses, as the objective function for optimizing the pressure ratio distribution. However, the inlet flow-path shape was determined under the assumption of inviscid flow. Therefore, when applying CFD, correction for a boundary layer displacement thickness was applied to the inlet baseline geometry.

The displacement thickness δ^* was estimated by integrating the differential equation for the momentum thickness θ along the upper wall surface and the cowl inner wall surface. Eq. 8 shows the equation for the two-dimensional flow case.

$$\frac{d\theta}{ds} + \theta \left[\frac{2 - M_e^2 + H_{12}}{M_e \left(1 + \frac{\gamma - 1}{2} M_e^2 \right)} \frac{dM_e}{ds} \right] = \frac{C_f}{2}$$
 (8)

The friction coefficient C_f used in the differential equations was calculated using the Van Driest II method [9]. The shape factor H_{12} , which is the ratio of the displacement thickness to the momentum thickness, was calculated using the Persh-Lee method [11]. This method assumes that the velocity distribution and temperature distribution within the boundary layer follow in accordance with the 1/n power law and the modified Crocco law, respectively.

$$\frac{u}{u_e} = \left(\frac{y}{\delta}\right)^{\frac{1}{n}} \tag{9}$$

$$\frac{T}{T_e} = \frac{\rho_e}{\rho} = \frac{T_W}{T_e} - \left(\frac{T_W - T_{aw}}{T_e}\right) \left(\frac{u}{u_e}\right) - \left(\frac{T_{aw} - T_e}{T_e}\right) \left(\frac{u}{u_e}\right)^2 \tag{10}$$

Here, the parameter n was calculated using the following approximation formula for the curve shown in Fig. 3 of Ref. [11].

$$n = -0.25831 Z^2 + 3.90952 Z - 4.81948, Z = log_{10} Re_{\theta}$$
 (10)

The boundary layer distributions were integrated to obtain δ^*/δ and θ/δ , and $H_{12} \equiv \delta^*/\theta$ was calculated from their ratio. The state variables at the boundary layer edge were calculated using values behind each shock wave obtained from the oblique shock wave relations. For the wall temperature, an isothermal wall at 700 K was assumed, as in the CFD discussion below. The differential equations were integrated using a fourth-order Runge-Kutta explicit method.

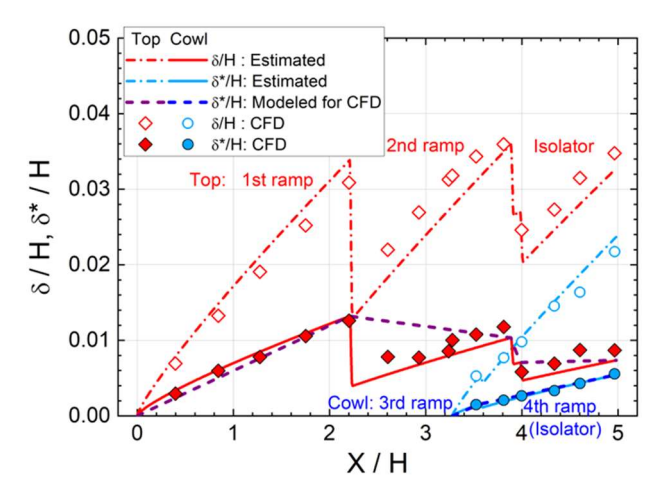


Fig 2. Estimated boundary layer thickness δ and displacement thickness δ^* , modeled δ^* for CFD, also shown are δ and δ^* evaluated from CFD results for validation: $P_{rat}=30$, I22, $\theta_e=-10$ deg.

Next, we describe the method of applying the displacement thickness correction obtained from the above calculations to the inviscid inlet baseline shape. Fig. 2 shows the predicted boundary layer thickness and displacement thickness for the upper wall and cowl inner wall in the case of an inlet with a two-stage external compression and two-stage internal compression configuration, I22 in Table 1. The design conditions are an overall pressure ratio of 30, flight Mach number of 6, and a dynamic pressure of 50 kPa. The displayed values are dimensionless values at inlet height H. The boundary layer grows as it progresses downstream from each leading edge of the upper wall and the cowl, with both boundary layer thickness and displacement thickness increasing monotonically. However, the flow is compressed abruptly at the upstream edge of each compression ramp and at the point where the inner shock wave impinges on the upper wall. Consequently, the boundary layer thickness and displacement thickness repeatedly decrease and then grow again each time they pass through these locations where the flow conditions change abruptly. Fig. 2 also shows the boundary layer thickness and displacement thickness read from the CFD results described later, represented by open symbols and closed symbols, respectively. The CFD results generally agree with the analytical solution, and the pattern of alternating increases and decreases in boundary layer thickness and displacement thickness was also observed in the CFD results. Therefore, the analytical solution can be considered valid. Next,

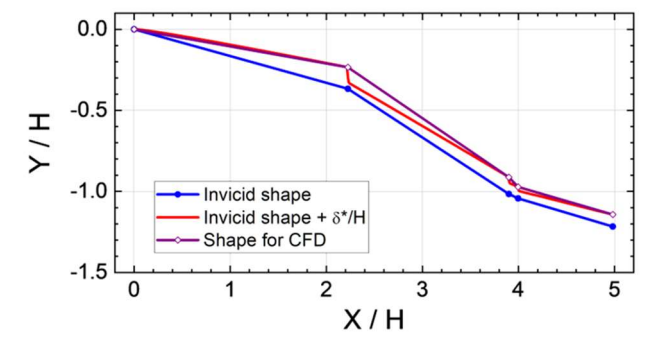


Fig 3. Comparison of top wall shapes with and without displacement thickness correction: P_{rat} =30, I22, θ_e =-10 deg. Note that amounts of displacement thickness correction in this figure are emphasized by a factor of 10 for clarity.

Fig. 3 shows the inviscid shape of the inlet upper wall and the shape with the displacement thickness correction applied. Note that the amounts of the displacement thickness correction applied are emphasized by a factor of 10 for clarity. As shown by a red line in Fig. 3, if the analytical solution for the displacement thickness were applied directly, the wall surface shape around each definition point of the inlet flow-path shape would exhibit a step-like discontinuity, similar to a forward-facing step, which would generate strong flow disturbances. To avoid this, the *Y*-coordinate of the inlet flow-path definition points, excluding the tips of the top and cowl walls, were shifted by the maximum value of the displacement thickness in their vicinity. The corrected top wall shape for CFD is shown by a purple

line with open diamond symbols. The amounts of the displacement thickness correction are also shown as thick dashed lines in Fig. 2. Fig. 4 shows the wall pressure distribution on the upper wall and cowl inner wall obtained from CFD simulations of the inlet shape with displacement thickness correction applied. The figure also displays the wall pressure values for each section assumed during the design of the inlet baseline shape. The CFD wall pressure distribution shows a slight downstream shift in the incidence position of the cowl tip shock wave near X/H=3.9 on the upper wall, resulting in a pressure drop due to the expansion wave. In addition, a localized pressure drop occurs in the isolator downstream of the inlet due to the incidence of the expansion wave. However, the wall pressures in each section are generally consistent with the assumed values. Based on this, the CFD evaluation applied this displacement thickness correction model to all inlet basic configurations.

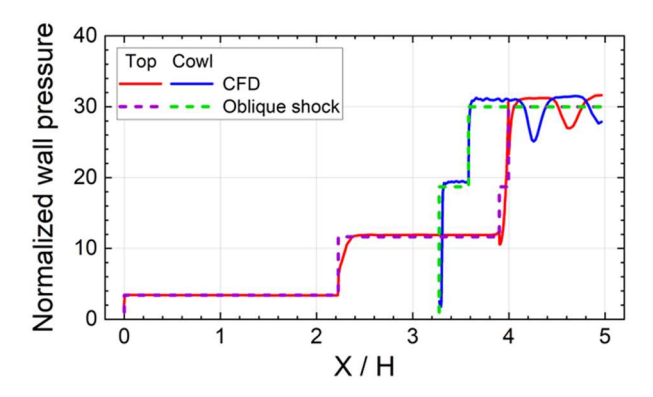


Fig 4. Normalized pressure distribution along top and cowl inner wall obtained by 2D RANS CFD: P_{rat} =30, I22, θ_e =-10 deg.

Note that this slight deviation in shock wave incidence position may be due not only to the incompleteness of the displacement thickness correction model, but also to the fact that while the inlet baseline shape study assumes a calorically perfect gas with constant specific heat ratio, CFD assumes a thermally perfect gas. This difference could cause the specific heat ratio to decrease due to temperature rise, potentially resulting in a slightly smaller shock angle with CFD.

2.4. CFD method

CFD evaluation was conducted using JAXA's in-house 2D RANS code. It supports multi-block structured grids and multi-component combustion gas flow analysis. The convection and viscous terms in the governing equations were differentiated using the AUSM-DV scheme [12] with MUSCL interpolation [13], and second-order central difference, respectively. In addition, since the objective was to obtain a steady-state solution, the LU-SGS implicit method [14] was used for the time integration method. The computational domain was assumed to be fully turbulent, and the k- ω SST model [15] was used as the turbulence model. A working fluid of air was treated as a thermally perfect gas with 21% oxygen and 79% nitrogen in mol.

As the initial condition, the freestream condition was applied throughout the entire computational domain. This is known as an impulsive start. This approach was chosen because the purpose of this study is to explore inlet geometries that could potentially represent the flow field at the inlet start state under low Mach number conditions, specifically the switching conditions between TRJ and SCRJ. It is widely known that applying an impulsive start to CFD simulations of scramjet inlet flow often predicts flow fields in the start state, even for inlet geometries that unstarts in wind tunnel tests. This occurs because the process of forming the inlet flow differs significantly between wind tunnel tests and CFD with the impulsive start. This study prioritizes achieving high efficiency and high compression ratios to attain high combustion efficiency in SCRJ combustors using jet fuel across a wide operating range. The approach aims to resolve inlet start-up achievement and stable maintenance by introducing a variable mechanism. Therefore, an impulsive start is suitable for the objective of the present study, as it reduces the risk of overlooking inlet shapes that possess a start-state solution of the SCRJ inlet.

An example of the computational grid is shown in Fig. 5. It is a two-dimensional structured grid with 301×150 grid points. The minimum grid width at the vicinity of the inlet wall surface is 5 micron, satisfying $y^+ < 1.5$. The freestream condition shown in Table 2 was given to the upstream boundary airflow condition. The downstream boundary within the inlet and beneath the cowl was set to an outflow

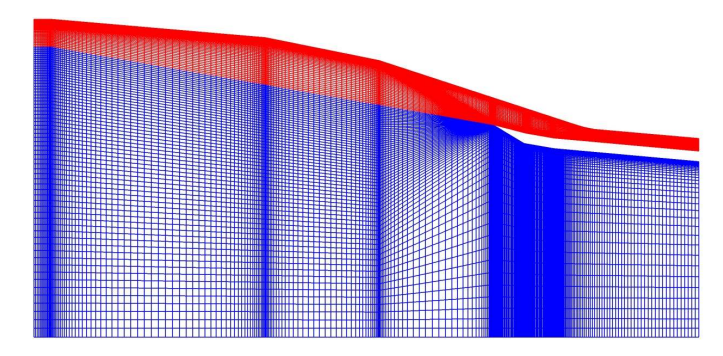


Fig 5. Example of a numerical grid for CFD

condition with zero-order extrapolation. Each wall surface of the inlet was treated as non-slip and assigned an isothermal wall condition with a wall temperature of 700 K.

3. Results and discussion

3.1. Design conditions

The subject of this study is designing the inlet for a SCRJ engine intended for installation on a 10- to 15-meter-class technology demonstrator [5], for which conceptual studies are being conducted within this research program. The current engine scale is defined by an inlet height of 0.6 m and an engine total length of 6 m. Therefore, the present study assumes an inlet height H of 0.6 m. The four compression stage configurations examined are shown in Table 1.

The inlet design point was set to be the cruise condition, typically at the highest Mach number within the operating range, expected to account for the majority of scramjet operation during the anticipated mission. Here, referencing the hypersonic transport market study [4], the design Mach number was set to 6. The flight dynamic pressure was set to 50 kPa, a commonly used value representing average scramjet operating conditions. The flow conditions at the design point, based on US Standard Air 1976, are shown in Table 2. Table 2 also includes the flow conditions for the off-design points evaluated later via CFD.

At the start of the design study, the overall pressure ratio of the inlet was set to 50 based on prior research by Smart [16]. In this case, the static pressure at the inlet exit for the design point would be 99.2 kPa, a static pressure value that sufficiently enables the achievement of supersonic combustion using jet fuel.

Relating to the design condition 3 mentioned above, the interval of the impinge points of the cowl ramp shock waves on the upper wall Δs was set to be 0.06 m (0.1H).

Conditions	Design	Off-design		
Flight Mach number	6	5	4	3.5
Flight dynamic pressure, kPa	50	50	50	50
Altitude, km	26.6	24.2	21.4	19.7
Static pressure, kPa	1.984	2.857	4.464	5.831
Static temperature, K	223.2	220.8	217.9	216.7
Velocity, m/s	1797	1489	1184	1033
Unit Reynolds number ×10 ⁻⁶ , m ⁻¹	3.82	4.65	5.91	6.81

Table 2. Flow conditions at design point and off-design points

3.2. GA optimized results of pressure ratio distribution and inlet baseline geometry

Fig. 6 shows the GA optimization results for pressure ratio distribution to each compression stage for the four compression configurations. The vertical axis shows the pressure ratio of each compression

stage, and the horizontal axis shows the stage number. For reference, the pressure ratios assuming even distribution of the pressure ratio among each stage in the external and internal compressions are shown as dashed lines. Although the GA optimization results showed some scatter, they all distributed near the pressure ratios assumed for the even distribution case. Moreover, even when the pressure ratio changes between external and internal compression due to differences in compression stage configuration, it remained to distribute near the pressure ratio value for the even distribution. Furthermore, the pressure ratio for each stage was nearly identical for both external and internal compression. These results were similar to the optimal distribution analytically determined by Smart [6] for inviscid flow.

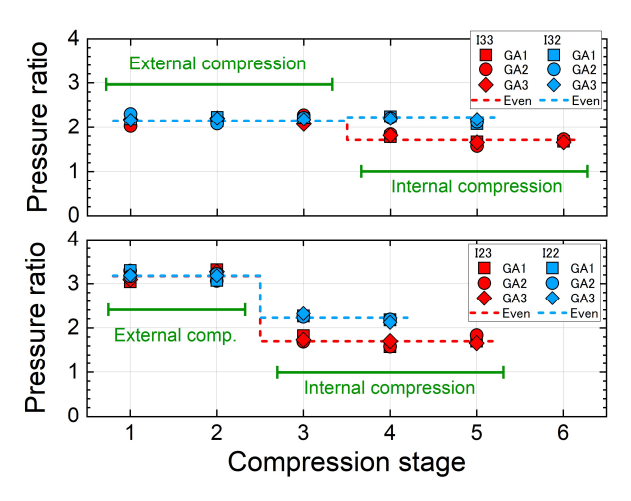


Fig 6. GA-optimized distribution of pressure ratio: P_{rat} =50, $\theta_e \sim 0$ deg.

Next, Fig. 7 shows the flow-path shapes corresponding to the pressure ratio optimization results for each compression stage configuration. The coordinates in each figure are dimensionless values based on the inlet height H. Each figure shows the results of three optimization calculations done under the same condition, which did not completely match. However, the variation in the shape definition points observed in Fig. 7 was primarily due to differences in the X-coordinate values, while the Y-coordinate values were nearly identical. Figs. 8 and 9 show the inlet exit height and total pressure recovery plotted against the total length of the inlet. Data points for the same compression configuration in these figures showed variation only along the horizontal axis representing the total inlet length, with the values themselves matching well. Therefore, it is possible that the cause of the discrepancy in the optimal solutions obtained under the same conditions, apart from deficiencies in the optimization program, is the high sensitivity of the X-coordinate values of the flow-path shape definition points to slight differences in the shock angle and airflow deflection angle, which appeared as relatively large differences in the calculation results.

Similar to Fig. 6, the inlet flow-path shapes assuming the even distribution of the pressure ratio are

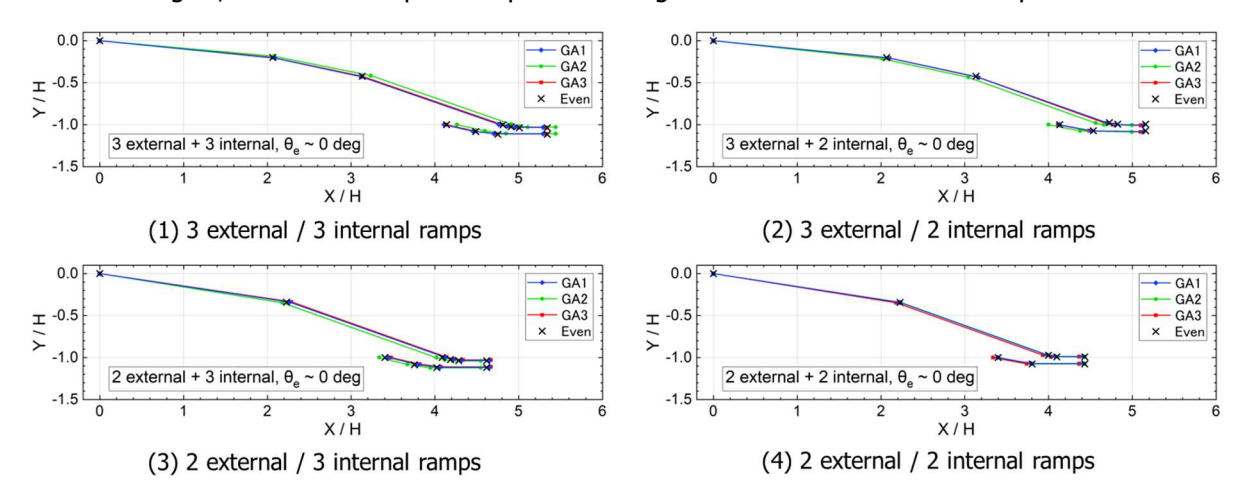


Fig 7. GA-optimized inlet geometries for inviscid flow: $P_{rat}=50$, $\theta_e \sim 0$ deg.

shown by black cross symbols for each compression configuration in Fig. 7. The inlet shapes for the even distribution case fell within the range of scatter observed in the inlet shapes determined by the GA-optimized pressure ratio distribution. The sole exception is the I32 case shown in Fig. 7(2), but it is presumed that this would also fall within the variation range if the number of optimization calculations were increased.

Based on the above, it was concluded that under the design conditions of this study, the effect of total pressure loss due to viscous effect is small, and the optimal pressure ratio distribution to each compression stage did not significantly differ from the distribution in the inviscid case.

3.3. Effects of compression stage configuration on inlet shape and performance

Next, we examined the effects of difference in the compression stage configurations on the inlet flow-path shape and its performance. Fig. 8 compares the total length and exit height of the inlet for each compression configuration. The total length was longest for the I33 configuration, which has three stages of both the external and internal compressions, while the shortest was for the I22 configuration, which has the fewest compression stages. Comparing I32 and I23, which have the same total number of stages, the I32 with three external compression stages is longer. Conversely, the exit height trend was opposite: I33 had the lowest exit height, while I22 had the highest. These results clearly showed that the total length of the inlet increases with the number of compression stages, particularly with more external compression stages. Since the overall pressure ratio was fixed in this study, increasing the number of compression stages weakens each shock wave, reducing the shock angle and consequently lengthening the inlet. Furthermore, while shapes with greater overall length had lower exit heights, this is also due to the weakening of each shock wave, which suppresses entropy increase and realizes smaller volume of the airflow .

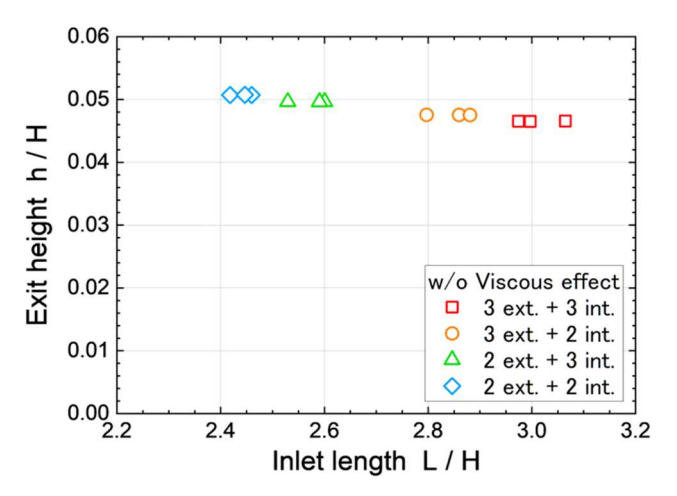


Fig 8. Inlet length and exit height: $P_{rat}=50$, $\theta_e \sim 0$ deg

Next, Fig. 9 shows the total pressure recovery for each compression configuration. The horizontal axis represents the inlet length. Fig. 9 displays the total pressure recovery calculated for each airflow condition at the inlet exit: one using the inviscid flow calculated with the oblique shock wave relation, and another incorporating viscous losses, namely wall friction and heat transfer to the wall. The total pressure recovery for both inviscid and viscous flow reached its maximum for I33, which has the most compression stages, and its minimum for I22, which has the fewest. Comparing I32 and I23, which have the same total number of stages, the value for I32, having more external compression stages, was larger. The total pressure loss for inviscid flow is the sum of the total pressure losses due to each oblique shock wave. In this design study, the overall pressure ratio was fixed as a design condition. Consequently, increasing the number of compression stages weakens individual shock waves, leading to an increase in the total pressure recovery. Next, the difference in total pressure recovery between inviscid and viscous flow represents the viscous total pressure loss. The viscous total pressure loss increased with the number of compression stages, particularly with more external compression stages. This occurred because increasing the number of compression stages weakens each shock wave and reduces the shock angle, resulting in a longer total length of the inlet and an increased wetted area of the airflow. In this study's results, the total pressure recovery considering viscous losses also reached its maximum for I33, which has the most compression stages and longest total length, and its minimum

for I22, which has the shortest total length, similar to the inviscid flow value. This indicates that, within the design condition range of this study, the dominant factor governing the difference in total pressure recovery between compression configurations was the difference in total pressure loss due to oblique shock waves, while the contribution of total pressure loss due to viscosity was small.

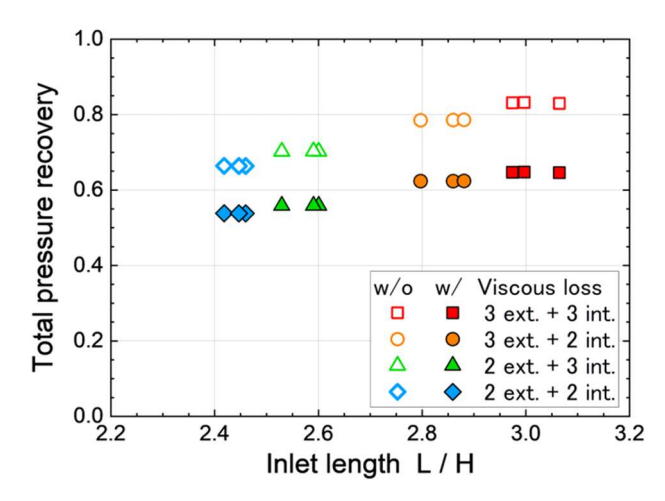


Fig 9. Total pressure recovery: $P_{rat}=50$, $\theta_e \sim 0$ deg.

3.4. Examination on existence of inlet start solutions under TRJ-SCRJ switching conditions using CFD

In the CFD evaluation, we first investigated whether the inlet geometry designed under M6 conditions possessed a starting solution under Mach 3.5, assumed TRJ-SCRJ switching conditions. Furthermore, previous investigations confirmed that the pressure ratio distribution and basic inlet geometry optimized by GA showed no significant difference compared to those with the even distribution. In the meantime, it was also found that the GA optimization results exhibited some scatters. To avoid the influence of the scatter in the GA-optimized shapes on the CFD evaluation results aimed at comparing inlet shapes, the inlet flow-path shape evaluated by CFD was derived from a inviscid baseline shape with the even distribution of the pressure ratio applied to both the external and internal compression stages, with the displacement thickness correction. The flow conditions used for the CFD evaluation, including off-design point ones, are listed in Table 2. For the compression stage configurations, evaluations were performed on the four configurations shown in Table 1 as much as possible. An isolator of the same length as the inlet height H was connected to the inlet exit. The isolator flow-path was designed as a constant-height parallel duct with displacement thickness correction applied. The exit orientation of the inlet was set to be parallel to the main flow, i.e., the exit angle θ_e =0 degrees. The angle of attack was 0 degrees.

First, the inlet flow-path shape designed for the overall pressure ratio of 50 was evaluated using CFD. However, flow fields for the starting state were only obtained down to the M4 condition, while the flow field for the M3.5 condition was in an unstart state. Therefore, the inlet was redesigned while gradually lowering the design pressure ratio to 40, 35, and 30, and this process of CFD evaluation was repeated. However, even after reducing the design pressure ratio to 30, we were unable to obtain the flow field for the starting state under the M3.5 condition.

Fig. 10 shows the Mach number contours for each airflow condition with a design pressure ratio of 30, compression configuration of I33, and θ_e =0 degrees. For the M6 condition shown in Fig. 10(a), the shock-on-lip condition, where the oblique shock waves formed by the external compression ramps impinge on the cowl leading-edge, was achieved. In the internal flow-path, oblique shock waves were formed near the cowl leading-edge by the internal compression ramp, causing the Mach number to gradually decrease. For the M5 and M4 conditions, the Mach number decrease caused the angle of the external shock waves to increase, shifting its position upstream. In the internal flow-path, the angles of the internal shock waves also increased. When those impinged on the upper wall, a reflected shock wave formed, but supersonic flow was maintained over a wide area. However, under the M3.5 condition, a subsonic region expanded around the position where the shock wave from the cowl compression impinged on the upper wall, resulting in an unstart-state flow field, as shown in Fig. 10(d).

To achieve high performance in the scramjet combustor, the overall pressure ratio of the inlet should

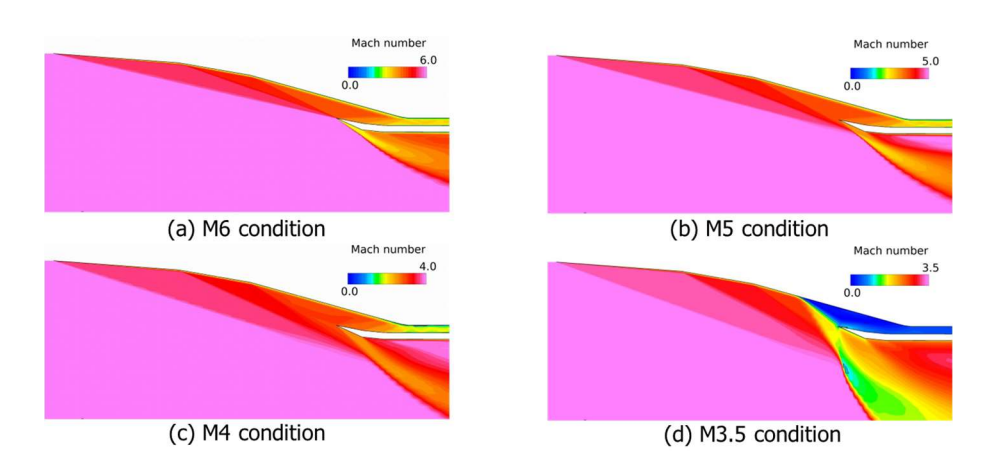


Fig 10. Mach number contours: P_{rat} =30, I33, θ_e =0 deg.

be maintained as high as possible. Therefore, we investigated methods to obtain the flow field in the start state under the M3.5 condition without reducing the inlet pressure ratio below 30. The start/unstart phenomenon of scramjet inlets is summarized by the relationship between the Mach number at the entrance of the internal compression section and its exit-to-entrance area ratio. Therefore, we considered reducing the proportion of internal compression while maintaining the design pressure ratio. Reducing the internal compression ratio causes the effect of deflecting the airflow downward due to external compression to dominate, resulting in the inlet exit airflow direction pointing downward relative to the main flow. From a design perspective, specifying the inlet exit direction facilitates shape control. Therefore, we added the airflow angle at the inlet exit θ_e as an inlet design parameter and determined the ratio between the external and internal compressions that matches the specified airflow angle. Here, the equal distribution of the pressure ratios of the compression stages belonging to either external compression or internal compression are assumed as before. The negative value of the inlet exit angle θ_e indicates that the airflow at the inlet exit goes downward.

With the design pressure ratio maintained at 30, inlet geometries were set with θ_e =-5 degrees and 10 degrees. CFD evaluation under the M3.5 condition showed that at -5 degrees, the start-state flow field were observed with the two compression configurations (I33 and I22), while at -10 degrees, the flow field in the start state for all the compression configurations. Fig. 11 shows the Mach number contours for the I33 compression configuration at θ_e =-10 degrees. Supersonic flow was maintained over a wide region of the internal flow-path even under the M3.5 conditions.

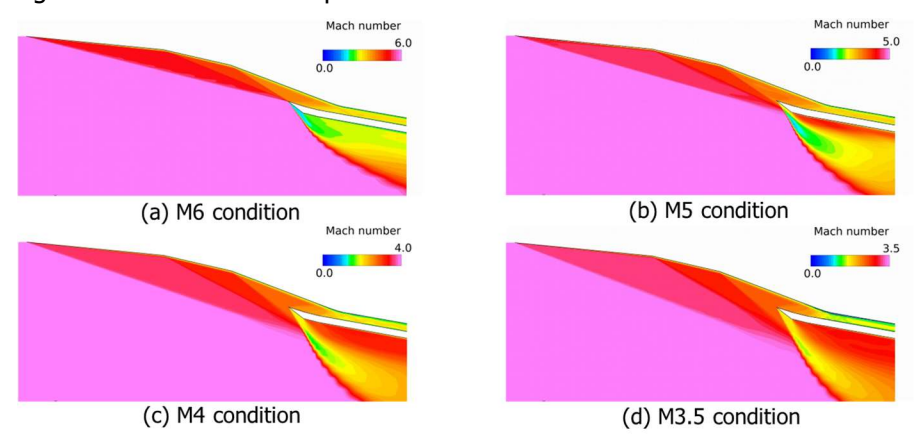


Fig 11. Mach number contours: P_{rat} =30, I33, θ_e =-10 deg.

To summarize the occurrence of the start and unstart states under M3.5 conditions, the start-state flow field was obtained at a design pressure ratio of 30, but only when θ_e was set to -5 degrees and -10 degrees. In addition, we evaluated increasing the design pressure ratio to 40 and 35 at θ_e =-10 degrees, but both resulted in an unstart state.

Fig. 12 shows a diagram organizing the conditions for start and unstart states under the M3.5 condition, based on the relationship between the Mach number at the entrance of the internal inlet and its exit-

to-entrance area ratio. Data points marked with open symbols indicate conditions where a start state was obtained. For reference, the figure also shows the reference curve based on Kantrowitz and isentropic criteria. Fig. 12 shows that cases where a start state solution was obtained occurred under conditions where the area ratio was large relative to the inlet Mach number—that is, where the exit area was large relative to the entrance area of the internal inlet, resulting in weaker internal compression and better starting performance. Therefore, the determination of the start and unstart state in this study was considered valid.

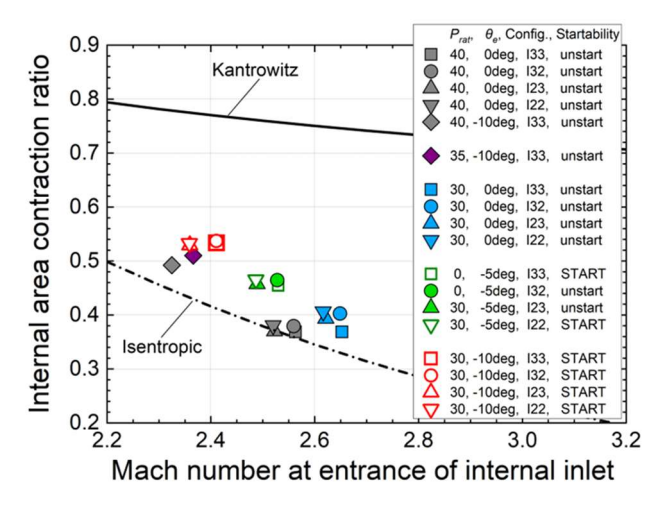


Fig 12. Inlet startability at M3.5 condition; shown with Mach number at the entrance of the internal inlet and the internal area ratio.

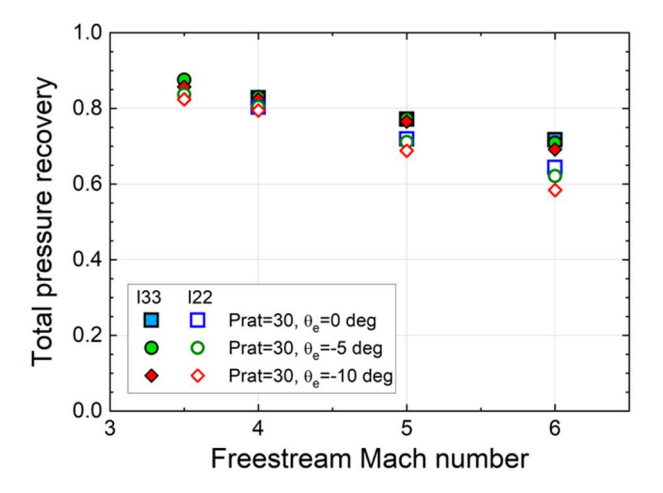


Fig 13. Total pressure recovery at inlet exit: I33 and I22, θ_e =0, -5, -10 deg.

3.5. Comparison of total pressure recovery for each compression stage configuration using CFD

Next, Fig. 13 shows the total pressure recovery at the inlet exit cross-section for I33 and I22. Results are shown for the overall pressure ratio of 30 and the exit angles θ_e of 0°, -5°, and -10°. Cases where only unsart solutions were obtained under the M3.5 condition were excluded. As previously mentioned, the total pressure recovery for I33 was higher than that for I22. This difference particularly increased at higher Mach numbers. Furthermore, for both I33 and I22, the total pressure recovery decreased as the exit flow angle became more downward. Additionally, the effect of the exit angle differences was greater for I22, which has fewer shock waves, than for I33. This occurs because when the exit flow direction matches the mainstream, the pressure ratio difference between the external and internal compression stages is small, resulting in minimal total pressure loss due to shock waves. However, when the exit flow is directed downward, the pressure ratio difference between the external and internal stages increases, particularly due to a larger pressure ratio in the external stage, leading to greater total pressure loss. Furthermore, this effect is more pronounced in I22, which has fewer stages. For I33, at θ_e =0°, the pressure ratio of the external compression stage is 1.18 times that of the internal

compression stage, showing little difference. However, at θ_e =-10°, the difference increases to 1.66 times. For I22, the difference is even more pronounced: at θ_e =0°, it was 1.30 times, but at θ_e =-10°, the difference increases to 2.13 times.

3.6. Comparison of inlet drag for each compression stage configuration using CFD

Finally, the drag forces imposed on each inlet were evaluated. The drag forces calculated via CFD for each inlet are shown in Fig. 14. The overall pressure ratio is 30, the compression configuration is I33 and I22, and the exit angle θ_e is 0 degrees, -5 degrees, and -10 degrees. However, cases where the inlet unstart occurred under the M3.5 condition are excluded. The "Total" shown in the upper row of Fig. 14 represents the sum of the drag forces in the axial direction acting on the upper wall and both side of the cowl wall. Within this, the 'Inner' shown in the middle row is the sum of the drag forces acting on the upper wall and the cowl inner wall, while the "Outer" shown in the lower row is the drag force acting on the cowl outer wall. The drag value shown in Fig. 14 was divided by the product of the freestream dynamic pressure and the inlet height H to obtain the drag coefficient.

First, the total drag coefficient was smallest under the design condition of Mach 6 and increased as the flight Mach number decreased. A notable difference was its significant variation with the exit angle θ_e , being smallest at θ_e =0 degrees and largest at θ_e =-10 degrees. These trends were common to both I33 and I22. Furthermore, the difference in drag between I33 and I22 was relatively small, and their relative magnitude varied depending on the exit angle. Next, the inner drag coefficient showed the same trend as the total drag coefficient, increasing as the flight Mach number decreased, but the difference due to variations in the exit angle was small. Conversely, the outer drag coefficient showed significant variation with the exit angle, and the difference in the total drag coefficient with the exit angle was primarily attributed to differences in the outer drag coefficient. In addition, while the difference in the outer drag coefficient between M6 (design cond.) and M5 was relatively large, the difference at low-speed conditions was comparatively small. Regarding the causes of this increase in the outer drag coefficient: at the design point, drag increases due to the greater angle of the external compression ramp and the downward-facing internal flow-path, which increases the angle of attack on the cowl outer surface. At the off-design points, in addition to the above reasons, the airflow capture rate decreases. Consequently, spillage drag from the airflow that could not be captured increases, further increasing the outer drag coefficient.

From the above discussion, we concluded that while the modified design with the inlet exit directed downward provides a solution for the start state conditions down to lower Mach numbers, it also significantly increases the drag imposed on the inlet, particularly the cowl outer drag.

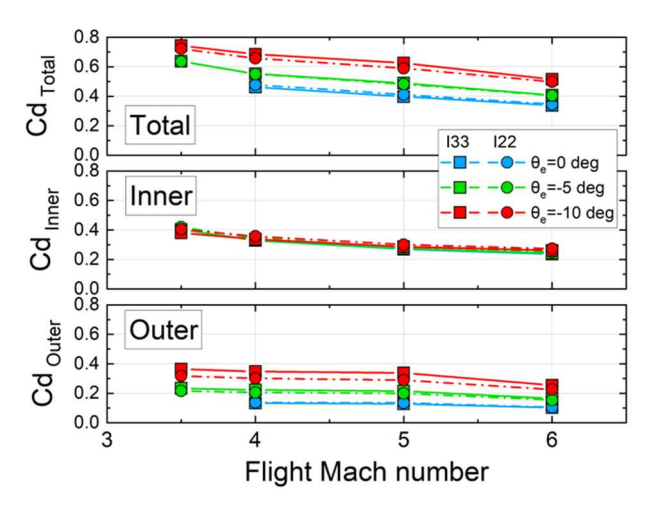


Fig 14. Drag coefficient; upper: total drag, middle: inner drag, lower: outer drag

4. Conclusions

The TBCC engine, combining a scramjet (SCRJ) engine capable of high-speed flight with a turbo-ramjet (TRJ) engine to provide thrust from takeoff to SCRJ operating conditions, is proposed for application to the propulsion system of a hypersonic cruise transport aircraft. Research and development of the key elemental technologies required for its realization is underway. A key technical challenge for the SCRJ

engine is extending its operating range down to lower speeds (expected between Mach 3 and 4) to enable seamless transition with the TRJ. The present study aimed to develop a design method for a SCRJ inlet capable of maintaining a start state flow field up to the switchover point with the TRJ, while achieving high total pressure recovery and compression ratio under cruise conditions. This involved optimizing the pressure ratio distribution of a two-dimensional multi-stage ramp mixed-compression type inlet and evaluating startability using CFD.

- The pressure ratio distribution to each compression stage and the inlet geometry of the 2D multi-stage ramp-compressed SCRJ inlet, optimized using GA with total pressure recovery rate considering viscous losses as the objective function, closely matched those obtained assuming uniform distribution for both external and internal compression. That is, the results were similar to the optimal distribution obtained in the inviscid flow case of Smart [6].
- Under the design conditions of this study, the difference in total pressure recovery due to the different compression configurations was primarily dominated by the difference in total pressure loss caused by oblique shock waves. Therefore, when the overall pressure ratio was given, the total pressure recovery rate was higher with more compression stages.
- Under the design conditions of this study, inlet flow field with a start state was obtained under the M3.5 condition by reducing the design pressure ratio to 30 and adopting a shape that allowed the airflow direction at the inlet exit to be 5 or 10 degrees downward, thereby decreasing the internal compression ratio. However, reducing the internal compression ratio significantly increased the drag force on the inlet. Among these, the increase in drag force on the cowl outer surface was particularly severe.

Acknowledgement

This work was supported by JST K Program Grant Number JPMJKP23E1, Japan.

References

- 1. Tomioka, S., et al.: 低軌道への再使用輸送系を目指したRBCC エンジンのシステム検討 (System Study on a RBCC engine for Re-usable Launch Vehicle to Low Earth Orbit), Proceedings of FY2012 Space Transportation Symposium, STCP-2012-036 (2012, in Japanese)
- 2. www.boeing.com/content/dam/boeing/boeingdotcom/features/innovation-quarterly/archive/IQ_2018_August.pdf
- 3. www.hermeus.com/halcyon
- 4. Deloitte consulting LPP.: Commercial Hypersonic Transportation Market Study. NASA Technical Reports Server. https://ntrs.nasa.gov/citations/20210014711. Accessed 1 August 2025.
- 5. Tomioka, S., et al.: 研究計画「幅広い作動域を有するエンジン設計技術の地上実証」について (On Research Plan Titled as Ground Test Validation of Engine Design Method with Wide Operation Range), Proceedings of the 68th Space Sciences and Technology Conference, 1J01 (2024, in Japanese)
- 6. Smart, M.K.: Optimization of Two-Dimensional Scramjet Inlets. J. Aircraft 36(2), pp.430-433 (1999)
- 7. Smart, M.K.: Design of Three-Dimensional Hypersonic Inlets with Rectangular-to-Elliptical Shape Transition, J. Prop. Power, 15(3), pp.408-416 (1999)
- 8. Musa et al.: New Parent Flowfield for Streamline-Traced Intakes. AIAA J. 61(7), pp.2906-2921 (2023)
- 9. Van Driest, E.R.: On Turbulent Flow Near a Wall, J. Aero. Sci. 23, pp.1007-1011 and 1036 (1956)

- 10. Hopkins, E.J., Inouye, M.: An Evaluation of Theories for Predicting Turbulent Skin Friction and Heat Transfer on Flat Plates at Supersonic and Hypersonic Mach Number, AIAA J. 9, pp. 993-1003 (1971).
- 11. Persh, J., A Theoretical Investigation of Turbulent Boundary Layer Flow with Heat Transfer at Supersonic and Hypersonic Speeds, NOL NAVORD Rep. 3854 (1955)
- 12. Wada, Y., Liou, M.-S.: A Flux Splitting Scheme with High-Resolution and Robustness for Discontinuities, AIAA paper 94-0083 (1994)
- 13. van Leer, B.: Towards the Ultimate Conservative Difference Scheme, V. A Second Order Sequel to Godunov's Method, J. Com. Phys.., 32, 101–136 (1979)
- 14. Yoon, S., Jameson, A.: An LU-SSOR scheme for the Euler and Navier-Stokes equations, AIAA J., 26 (9), pp.1025-1026 (1988)
- 15. Menter, F.R.: Zonal Two Equation k-omega Turbulence Models for Aerodynamic Flows, AIAA Paper 1993-2906 (1993)
- 16. Smart, M.K.: How Much Compression Should a Scramjet Inlet Do?, AIAA J. 50, pp.610–619 (2012).